Linear Dual-Series Mach Zehnder Modulator Employing Electrostatic Doping for Photonic Integrated Circuits

Subhradeep Pal ⓘ, *Member, IEEE*, and Sumanta Gupta ⓘ

Abstract—**In this paper, we propose a highly linear electrostatic doping (ED) assisted dual series Mach-Zehnder modulator (MZM) suitable for photonic integrated circuits (PICs). A complete simulation study on the performance of the proposed dual series MZM is incorporated in this paper. We have analytically formulated the steady-state and the nonlinear performance of the proposed modulator and the simulation results using commercial grade photonic circuit simulator are also incorporated in support of the analytical study. Simulation results show that the proposed modulator can offer ∼16 dB of static extinction ratio (ER) with 3.2 dB of insertion loss (IL). The modulator offers approximately 10.2 dB of dynamic ER at 10 Gb/s data rate. The effect on the transfer function of the dual-series MZM due to the imbalance in the driving RF signals is also discussed supported with simulation results. The nonlinear performance of the proposed modulator is also estimated using analytical method and dual-tone test method. Results indicate that the spurious free dynamic range (SFDR) of the proposed dual series MZM for second and third order intermodulation distortions (IMD2 and IMD3) are 96.11 dB.Hz$^{1/2}$, and 132.4 dB.Hz$^{2/3}$, respectively. Study of the transient performance also reveals that the 3-dB electro-optic bandwidths are 11.39 GHz and 8.32 GHz for single and dual-series ED-assisted MZM, respectively.**

Index Terms—**Electrostatic doping, intensity modulation, mach-zehnder modulator, plasma dispersion effect, SFDR.**

I. INTRODUCTION

ONE of the biggest challenges in the modern data center is to manipulate and transport a large amount of data, which originates primarily because of intra-data center traffic [1]–[3]. Optical interconnect technology has the potential to address the requirements of enormous bandwidth, energy efficient and, low cost data transmission. As a result the optical interconnects are gradually replacing their electrical counterpart for short haul communication [1], [4]. With the enhanced application of optical interconnects, the search for ultra-small energy efficient integrated modulators suitable for photonic integrated circuits (PICs) has also soared. In PICs, two widely used intensity modulators on silicon platforms are Mach-Zehnder modulator

(MZM) and microring modulator (MRM) [5]–[8]. Although silicon MRM offers a very high extinction ratio (ER) and low device footprint, its performance is severely dependent on operating wavelength (λ) and temperature [9]–[11]. On the other hand, silicon based MZM suffers from large device footprint and significant power consumption [12]–[14]. To reduce the footprint of MZM, compact and highly efficient optical phase shifters (PS) are required. To increase efficiency and scale down the dimension of the PS, the general practice is to increase the doping level in the active region of the PS, which is generally a PN or PIN diode [15], [16]. It is very important to note that the increment in doping concentration in the device's active region also introduces problems like random dopant fluctuations (RDF), undesired dopant activation, variation in doping concentration etc [17], [18]. To get rid of these problems in active silicon photonic devices, recently we have proposed and analyzed electrostatic doping (ED) assisted intensity modulators [19]–[21]. We have also investigated ED-assisted optical PS loaded MZM which utilizes the free carrier plasma dispersion effect (FCD) [22], [23]. In these modulators, applied bias voltage (V_{bias}) induces excess free charge carriers inside the device's active region resulting a perturbation in effective refractive index (Δn_{eff}) and loss coefficient ($\Delta \alpha$). As mentioned in [20], both Δn_{eff} and $\Delta \alpha$ changes nonlinearly with V_{bias} and thus the output modulated signal from ED-assisted optical PS loaded MZM has a nonlinear relationship with V_{bias}.

Integrated silicon MZM generally has a nonlinear (more precisely sinusoidal) transfer function. For linearized operation, these modulators are often biased at approximately the linear portion of the sinusoidal transfer function and the input signal amplitude is maintained to a smaller value so that the optical modulators operate approximately linearly. The linearized silicon MZM finds wide applications in the area of optical analog links [24]–[26], microwave photonics [25], [27], generation of advanced modulation formats like PAM-4 [28], etc. However, realizing linear MZM over silicon, which has zero linear electro-optic coefficient, is more challenging than realizing standard lithium-niobate (LiNbO3) based MZMs. Compared to single MZM, dual-series MZM or dual-parallel MZM produces lower third-order distortion [24], [25], [29]. Cascading an MZM having higher ER with another MZM having reduced ER often offers a highly linearized modulator. Compared to dual-parallel MZM, dual-series MZM offers design advantages by avoiding power splitting/combining operation in optical domain [24]. However,
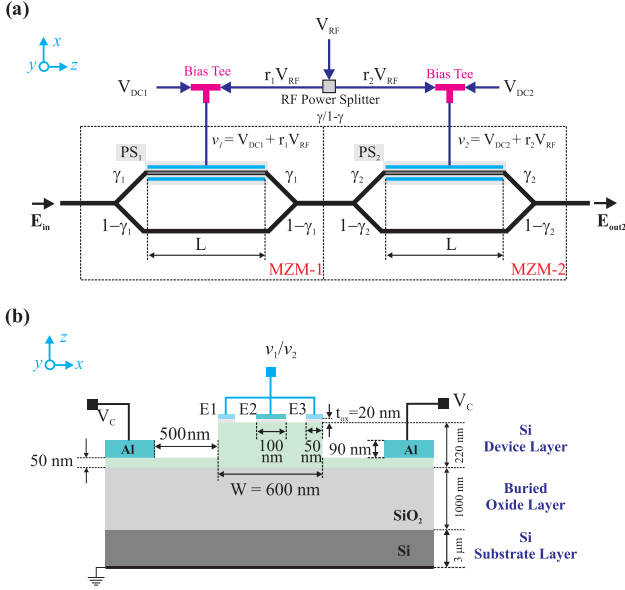
Fig. 1. Schematic representation of the proposed dual series MZM: (a) complete schematic; (b) cross-sectional view of a single ED-assisted PS loaded MZM.

dual series MZM requires critical control over bias voltages to reduce intermodulation distortions (IMDs). This configuration also introduces approximately 6 dB penalty in the noise figure compared to a single MZM [24]. In this paper, we propose and analyze the performance of a dual series MZM based on ED-assisted PS loaded MZM. The nonlinear performance of the proposed MZM is studied using both analytical and simulation methods.

The outline of the paper is as follows. Section II, describes the structure of the proposed dual-series MZM, the formulation of the device transfer function, and an analytical model of the non-linear distortion of the proposed modulator. In Section III, we present the simulation results for the proposed modulator. Finally, in Section IV we conclude.

II. PROPOSED DUAL SERIES ED-ASSISTED MACH-ZEHNDER MODULATOR

A. Device Description

The schematic diagram of the proposed ED-assisted dual series MZM is shown in Fig. 1. The input RF signal (V_{RF}) is first divided into two parts using an RF power splitter whose power splitting ratio equals to r_1/r_2. Both the RF signals are then provided into two bias tees where the signals are combined with suitable DC bias voltages V_{DC1} and V_{DC2}, respectively. The two output signals of the bias tees are used to drive two cascaded sub-MZMs (MZM-1 and MZM-2). A continuous wave laser source with optical power P_{in} (field E_{in}) and operating at wavelength λ is connected at the input of the proposed modulator. The cross-sectional schematic of a single optical PS is shown in Fig. 1(b). Both sub-MZMs use ED-assisted optical PS in an interferometric structure to achieve optical intensity modulation as per the applied electrical signal. The choice of materials for electrodes E1, E2, and E3 is purely based on work-function

(ϕ_m) of the metals. As discussed in [30], the suitable metals for anode and cathode electrodes are determined by the relation, $\phi_m > \chi_{Si} + 0.5E_g$, and $\phi_m < \chi_{Si} + 0.5E_g$, respectively. Typically, $\chi_{Si} = 4.17$ eV and, $E_g = 1.12$ eV resulting the required value of $\phi_m > 4.73$ eV for anode and $\phi_m < 4.73$ eV for cathode. Thus, some of the suitable metals for anode are Au, Pt, Pd, Ni, Co, W, Ag etc. Similarly, Gd, TiW, Zr, Al, Ta are few choices for cathode. Among these we have chosen Al for the two controlling electrodes present in pad region of the rib waveguide. Also, Au is chosen for electrodes E1 and E3 and Ag for electrode E2. Although the Au is not a CMOS-process friendly metal but the effective r.i. perturbation as well as modal attenuation factor due Au based electrodes is better compared to different other metal combinations. The effect of choosing different electrode metals will be discussed later in this paper. The dimension of the electrodes are also optimized to have better $V_\pi L$ product of each sub-MZMs as discussed in [20]. As per the Fig. 1(b), the two Al-based controlling electrodes are connected to -2 V DC supply, i.e. $V_C = -2$ V, while the electrodes E1-E2-E3 are connected to driving signal v_1/v_2. To achieve a highly linearized operation we have varied the RF power splitting ratio (r_1 and r_2) and length (L) of the both sub-MZMs. It is very important to note that the proposed optical PS consists of metal electrodes on the top of rib-waveguide making it a hybrid-plasmonic waveguide as discussed in [31], [32]. It is assumed that the proposed modulator will be operated only in TE mode.

B. Analytical Formulation of n_{eff} and Δn_{eff} for the ED-Assisted Optical Phase Shifter

The proposed dual-series MZM has one ED-assisted optical PS embedded in each sub-MZMs. It is imperative to formulate an analytical expression for estimating the perturbation in n_{eff} in the ED-assisted optical PS. Assuming the unperturbed r.i. of the Si waveguide is n_{Si} and the uniform doping concentration inside the rib waveguide, n_{eff} can be written as [33],

$$n_{eff} = \frac{\iint_{WG} n(x,y) |E(x,y)|^2 \, dS}{E_0^2} + C_1 \tag{1}$$

where E_0 denotes a normalizing constant; C_1 represents the integral outside the rib-waveguide and it is independent of voltage and doping concentration. Typically the guided optical TE mode in the proposed ED-assisted optical PS has the highest intensity at the center and decaying as the distance from the center increases. Such king of modal distribution of the electrical field inside the rib-waveguide can be approximated as $E(x,y) = \cos(k_x x)\cos(k_y y)$ [see Fig. 2(a)]. Here k_x and k_y are the optical propagation constants in transverse directions. Assuming the origin point at the center of the waveguide as depicted in Fig. 2(c), (1) can be extended as,

$$n_{eff} = \frac{1}{E_0^2} \int_{-\frac{W}{2}}^{\frac{W}{2}} \left[\int_{-\frac{h}{2}}^{\frac{h}{2}-\Delta h} n_{Si} \cos^2(k_y y) dy \right] \cos^2(k_x x) dx$$

$$+ \frac{1}{E_0^2} \int_{-\frac{W}{2}}^{\frac{W}{2}} \left[\int_{\frac{h}{2}-\Delta h}^{\frac{h}{2}} n_{PN} \cos^2(k_y y) dy \right] \cos^2(k_x x) dx + C_1 \tag{2}$$
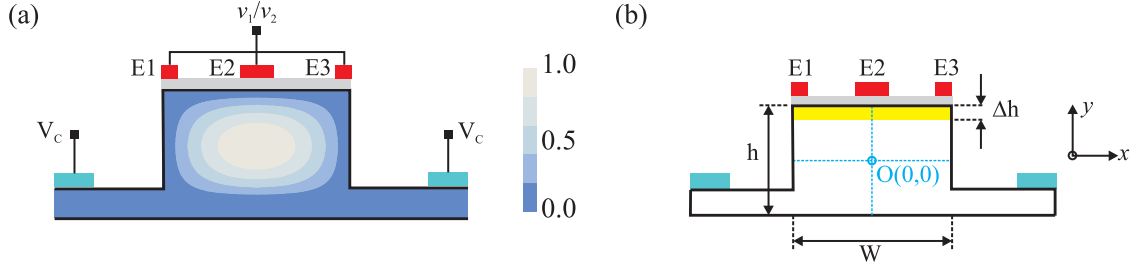
Fig. 2. Schematic illustrating optical TE mode profile inside the rib-waveguide of the proposed ED-assisted optical PS: (a) modal profile used for analytical formulation of n_{eff} of the rib-waveguide; (b) geometrical dimensions and co-ordinate system used for the analytical formulations. Note, the yellow region with height Δh at the bottom of the electrodes E1, E2, E3 indicate the inversion layer due to electrostatic doping.

$$n_{eff} = \frac{1}{8E_0^2}\left(W + \frac{\sin(k_x W)}{k_x}\right)\left[\Delta n\left(2h' + \frac{\sin(k_y h)}{k_y}\right.\right.$$
$$\left.\left. + \frac{\sin(k_y h'')}{k_y}\right) + 2n_{PN}\left(h + \frac{\sin(k_y h)}{k_y}\right)\right] + C_1 \quad (3)$$

where Δh is the region where carrier are accumulated due to ED effect, n_{PN} is the average r.i. of P-type and N-type Silicon. The value of Δh changes with the applied bias voltages in the electrodes E1, E2, and E3. Solving (2), yields the compact expression for n_{eff} which is mentioned in (3). In (3) it is assumed that, $\Delta n = n_{Si} - n_{PN}$, $h' = h - \Delta h$ and, $h'' = h - 2\Delta h$. Collecting terms related with h from (3) also yields,

$$n_{eff} \propto \Delta n\left(2h' + \frac{\sin(k_y h)}{k_y} + \frac{\sin(k_y h'')}{k_y}\right)$$
$$+ 2n_{PN}\left(h + \frac{\sin(k_y h)}{k_y}\right) \quad (4)$$

Since n_{eff} term depends strongly with the applied bias voltage v, the perturbation in n_{eff} estimated w.r.t v can be calculated as,

$$\Delta n_{eff}(v) = K_1(A_1 N_D^{1.011} + B_1 N_A^{0.838})$$
$$\times \left(h'(v) - h'(0) + \frac{\sin(k_y h''(v)) - \sin(k_y h''(0))}{k_y}\right) \quad (5)$$

where $A_1 = 5.4 \times 10^{-22}$ cm^3, and $B_1 = 1.53 \times 10^{-18}$ cm^3 at 1550 nm, and the constant term K_1 can be obtained from fitting. Likewise the optical absorption can also be estimated.

C. Estimation of Device Transfer Function

Refer to Fig. 1. The transfer function of the two sub-MZMs can be expressed as,

$$E_{out1} = E_{in}\left[\sqrt{1-\gamma_1}e^{-j\phi_0}e^{-\alpha_0 L} + \sqrt{\gamma_1}e^{-j\phi(v_1)}e^{-\alpha(v_1)L}\right] \quad (6a)$$

$$E_{out} = E_{out1}\left[\sqrt{1-\gamma_2}e^{-j\phi_0}e^{-\alpha_0 L} + \sqrt{\gamma_2}e^{-j\phi(v_2)}e^{-\alpha(v_2)L}\right] \quad (6b)$$

where $\alpha(v)$ and α_0 are the loss coefficients at biased and unbiased conditions, respectively. Similarly, $\phi(v)$ and ϕ_0 are

the phase associated with electric fields in the upper arm and the lower arm of the sub-MZM, respectively. In the above expressions, the output electric field after MZM1 and MZM2 are considered as E_{out1} and E_{out}, respectively. For the proposed dual series MZM, the input driving voltage in the two MZMs can be expressed as,

$$v_i = r_i V_{RF} + V_{DC,i}, \text{where } i = 1, 2 \quad (7)$$

Simplifying (6b), and assuming $\gamma_1 = \gamma_2 = 0.5$, we find the output field of the proposed modulator as,

$$E_{out} = E_{in}\left[1 + e^{-\Delta\alpha_1 L}e^{-j\Delta\phi_1} + e^{-\Delta\alpha_2 L}e^{-j\Delta\phi_2}\right]e^{-2j\phi_0}e^{-2\alpha_0 L}$$
$$+ E_{in}\left[e^{-(\Delta\alpha_1+\Delta\alpha_2)L}e^{-j(\Delta\phi_1+\Delta\phi_2)}\right]e^{-2j\phi_0}e^{-2\alpha_0 L} \quad (8)$$

where $\Delta\alpha_i$ and $\Delta\phi_i$ are the optical loss and phase perturbations due to FCD effect and are defined as,

$$\Delta\alpha_i = \alpha(v_i) - \alpha_0 \quad (9a)$$
$$\Delta\phi_i = \phi(v_i) - \phi_0 \quad (9b)$$

Generally in MZMs are operated at their quadrature transmission points and to have a strong electro-optic response, the amplitude of the RF signal and DC bias voltages should be made equal [29]. However, if such a condition is maintained, the nonlinear dependence of Δn_{eff} and $\Delta\alpha$ with the V_{bias} will also result in significant IMD in the output signal.

D. Nonlinear Performance Analysis

Generally to study the nonlinear performance of the modulator experimentally, one has to perform dual-tone test [34], [35]. In this sub-section we also employ a similar method to estimate the nonlinear performance of the proposed modulator analytically. A detailed mathematical analysis of the used method is well discussed in [29] and thus we have not included the same in this paper. Intrinsic loss of the Si-waveguide is almost 3 dB/cm at 1550 nm [36]. The proposed ED-assisted phase shifter with $t_{ox} = 60$ nm will offer a modal attenuation of 14.23 dB/cm at 2 V for TE mode. Thus, loss introduced by the FCD effect in the ED-assisted PS of length 500 μm and 775 μm are 0.71 dB and 1.10 dB, respectively. However, it is important to note that such a loss can be further compensated with the proper adjustment of power splitting ratios (i.e. γ_1 and γ_2) of the MZM. This is also confirmed from the simulation

results as shown in the Section III. Furthermore in dual series combination we have another parameter RF power splitting ratio (γ) that can be controlled to get even lesser IL. If we consider v_i and L to be small enough then, we can safely neglect the optical loss coefficients due to the FCD effect and intrinsic loss of the silicon waveguide. Typically, the driving RF signal power level lies within the range of 10 dBm to 14 dBm, which corresponds to a peak-to-peak amplitude level in between 2 V to 3.2 V for a 50 Ω matched load at 28 Gb/s. In such cases (8) can be simplified as,

$$E_{\text{out}} \simeq \frac{E_{\text{in}}}{4} \left[1 + e^{-j\Delta\phi_1} + e^{-j\Delta\phi_2} + e^{-j(\Delta\phi_1 + \Delta\phi_2)} \right] e^{-2j\phi_0} \tag{10}$$

Now assuming the input RF signal comprises of dual tone signals i.e. $V_{RF}(t) = v_0(\cos\omega_1 t + \cos\omega_2 t)$, the amplitude coefficients of the fundamental and third harmonic components are given by,

$$C_{FH} = \frac{k_0 k_1 L}{4} (r_2 - r_1) \tag{11}$$

$$C_{IMD3} = \frac{3v_0^3}{16} \left[\frac{(k_0 k_1 L)^3}{6} (r_1^3 - r_2^3) - k_1 k_2 (r_1^2 r_2 \right.$$
$$\left. + r_1 r_2^2) (k_0 L)^2 \right] + \frac{3v_0^3}{16} \left[k_3 (r_2^3 - r_1^3) k_0 L \right] \tag{12}$$

where $k_0 = 2\pi/\lambda$ is the free space wavenumber. The coefficient k_1, k_2, k_3, and k_4 are the fitting polynomial coefficients as described below,

$$\Delta n(v) = k_4 v^4 + k_3 v^3 + k_2 v^2 + k_1 v = \sum_{l=1}^{4} k_l v^l \tag{13}$$

From (12), it is clear that the IMD3 component of the proposed modulator is a function of RF power splitting coefficients (r_1 and r_2), the length of the modulator (L), input RF signal amplitude (v_0) and, operating wavelength (λ). For a given modulator length L with a known relation of $\Delta n(v)$, it is possible to minimize or even nullify the IMD3 component of the output modulated signal substantially using the following relation.

$$k_1^3 k_0^2 L^2 - 6k_0 k_1 k_2 L \left[\frac{r_1^2 r_2 + r_1 r_2^2}{(r_1 - r_2)(1 + r_1 r_2)} \right] - 6k_3 = 0 \tag{14}$$

The corresponding power of the fundamental and IMD3 component are calculated using the relation, $P_{FH} = 0.5 P_{\text{in}}^2 C_{FH}^2$, and $P_{IMD3} = 0.5 P_{\text{in}}^2 C_{IMD3}^2$, where P_{in} is the launched power of the continuous wave (CW). We have used these analytical formulations to predict the nonlinear performance of the proposed modulator.

III. SIMULATION RESULTS

In this section, we briefly describe the methodology used to estimate the performance of the proposed modulator. We also present the estimated DC transfer function along with its steady state performance, nonlinear performance and, the transient performance of the proposed modulator.
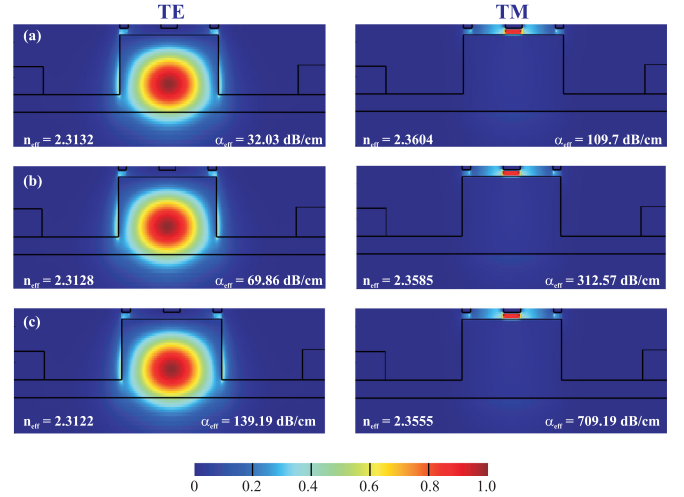

Fig. 3. Simulated modal profiles of the proposed ED-assisted optical PS at different bias voltages: (a) 0 V; (b) 2 V; (c) 4 V. Design parameters are $t_{ox} = 20$ nm, $W = 600$ μm, electrode combination is Au-Ag-Au.

A. Simulation Methodology

For simulating the performance of the proposed device, we have used the same design parameters of the noble electrode based MZM as discussed in [20]. Also, we have ensured that both MZM-1 and MZM-2 are identical. The carrier information inside the rib waveguide is numerically extracted at different bias voltages using a commercial-grade device simulator, which self-consistently solves the Poisson and drift-diffusion equations (ANSYS Lumerical Device CT R2022) [37]. Using the carrier information, change in refractive index (Δn) and change in loss coefficient ($\Delta\alpha$) at 1550 nm can be obtained from the modified Soref's relation [22],

$$\Delta n = -5.4 \times 10^{-22} \Delta N_e^{1.011} - 1.53 \times 10^{-18} \Delta N_h^{0.838} \tag{15}$$

$$\Delta\alpha = 8.88 \times 10^{-21} \Delta N_e^{1.167} + 5.84 \times 10^{-20} \Delta N_h^{1.109} \tag{16}$$

where ΔN_e and ΔN_h are the changes in electron and hole concentration per cc, respectively. Using the estimated value of Δn and $\Delta\alpha$, and (6b) we have estimated the static transfer function of the proposed modulator. Fig. 6 illustrates the variation of Δn and $\Delta\alpha$ with V_{DC}. For the estimation of nonlinear performance of the proposed modulator we have used (11) and (12).

B. Choice of Electrode Metals and Modal Analysis of ED-Assisted Optical PS

As shown in Fig. 1(b), three electrodes (E1, E2, and E3) are placed on the top of rib waveguide and a thin oxide layer is present between the electrodes and rib waveguide. The structure will exhibit plasmonic behaviour due to these metallic electrodes. The simulation results also confirms the same. The modal profile for the ED-assisted optical PS with electrode combination Au-Ag-Au is shown in Fig. 3. It is important to note that in hybrid plasmonic waveguide structures, guided TE mode offers small modal attenuation coefficient compared to the guided TM mode. This is because the guided TM mode lies inside the thin oxide layer whereas the guided TE mode lies inside the rib
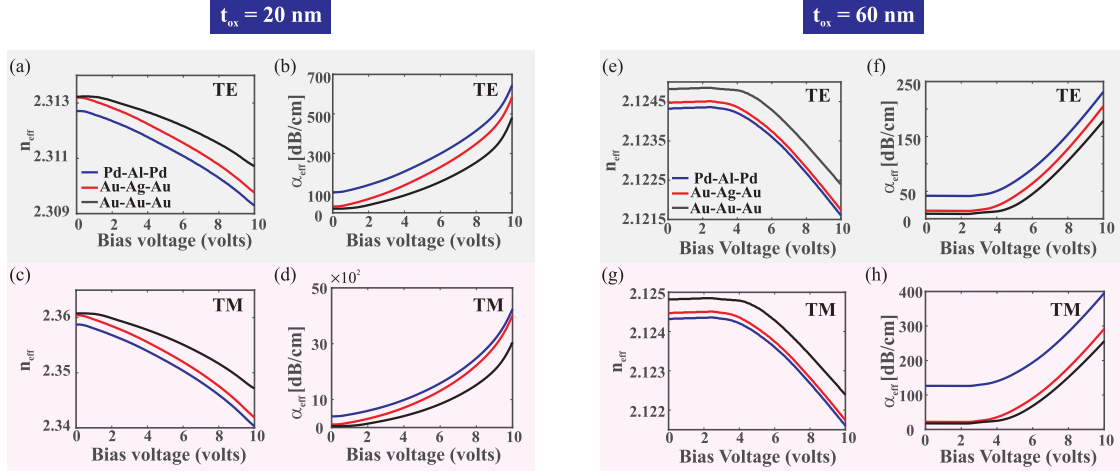
Fig. 4. Estimated modal n_{eff} and α_{eff} for the proposed ED-assisted optical PS with different t_{ox} and different metal combinations for the electrodes E1, E2, and E3.
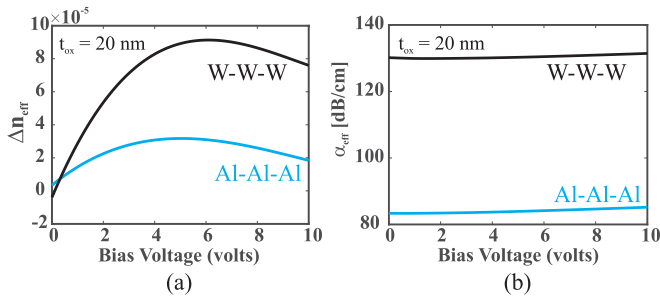

Fig. 5. Estimated value of Δn_{eff} and α_{eff} of the guided TE mode in the ED-assisted optical PS with waveguide width = 600 nm and $t_{ox} = 20$ nm for different metals in electrodes E1-E2-E3. Al: Aluminium. W: Tungsten.
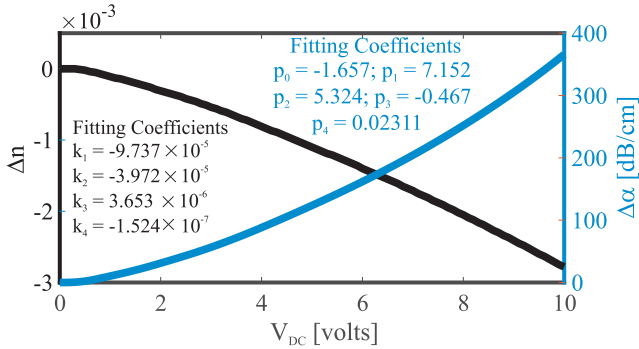

Fig. 6. Variation of Δn and $\Delta \alpha$ inside the rib waveguide with varying DC voltage. Fitting coefficients as mentioned in Section II is also listed.

waveguide. Also from the simulation results as illustrated in Fig. 3, the modal loss-coefficient is found to be significantly higher in TM mode compared to the guided TE mode. Thus in this paper, it is assumed that the proposed dual-series MZM will be operated only in TE mode to avoid significant modal loss due to the localized surface plasmonic resonance (LSPR) around the rib waveguide. However, it is interesting to note that the modal loss-coefficient changes significantly with the dimensions of the rib waveguide (W), oxide layer thickness (t_{ox}). As discussed

in [20], modal loss coefficients decreases with increasing values of W and t_{ox}. A similar optimization analysis as mentioned in [20], reveals the optimized value of W is 600 nm.

The choice of metal for the electrodes E1, E2, and E3 has a direct impact on the device footprint and, the performance metrics of the proposed dual-series MZM. A low perturbation in n_{eff} would lead to larger device footprint, while higher values of α will lead to high device insertion loss (IL). Also, from the standard CMOS fabrication technique point of view, some metals are not compatible with the CMOS process flow despite of their excellent potential in ED. Thus, choosing the metals for the electrodes E1, E2, and E3 for the ED-assisted optical PS should be done carefully. Among the various potential metals for the electrodes, we had chosen the controlling electrodes to be made of Al. As Al offers $\phi_m = 4.28$ eV making suitable for piling up the electrons underneath the both controlling electrodes. As the electrons pile up under the controlling electrodes, the refractive index under the controlling electrodes reduces (since electron pile up forces the hole concentration to decrease and thereby reduces the refractive index under the controlling electrodes). This perturbation in refractive index helps the guided optical mode to be confined within the central rib region even with the applied bias voltages on the electrodes E1-E2-E3.

As we want to achieve a perturbation in the n_{eff} of the guided optical mode, the metals of the electrodes (E1, E2, E3) should be chosen such a way that it should be able to create strong inversion layer underneath the electrodes in the p-type rib waveguide. Therefore the considered metals for the electrodes should have $\phi_m > 4.73$ eV and few of the plausible choices for the same are Pt, Pd, Au, Ag, W etc. We have considered various metal combination of the electrodes and studied the performance of the ED-assisted optical PS in terms of Δn and $\Delta \alpha$ as a function of V_{DC} with $t_{ox} = 20$ nm. From the simulation results as depicted in Fig. 4, it is clear that α_{eff} in TM mode is significantly higher compared to TE mode and the losses of the both the modes increase as t_{ox} reduces. The result also reveals that the noble metal (Au, Ag) based electrodes in optical PS offers significantly lower modal attenuation coefficient in both TE and
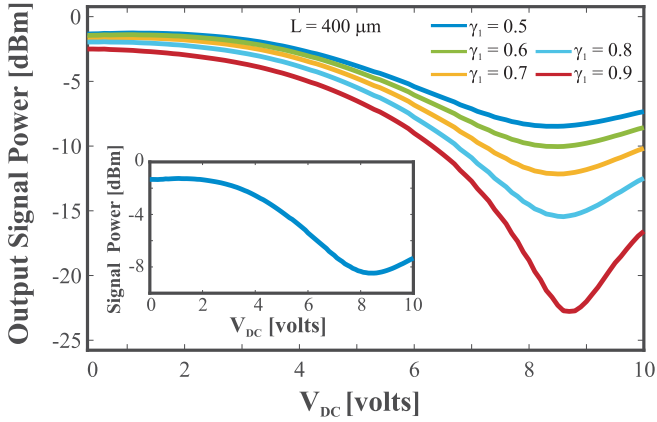
Fig. 7. Estimated DC transfer function of MZM-1 with varying γ_1 at the input section. Inset: zoomed transfer function of the sub-MZM for $\gamma_1 = 0.5$.
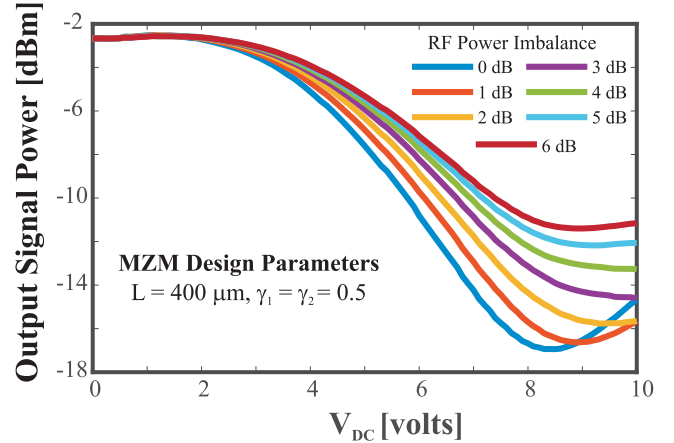

Fig. 8. Estimated DC transfer function of the proposed dual-series MZM with varying RF power imbalance between the two sub-MZMs.
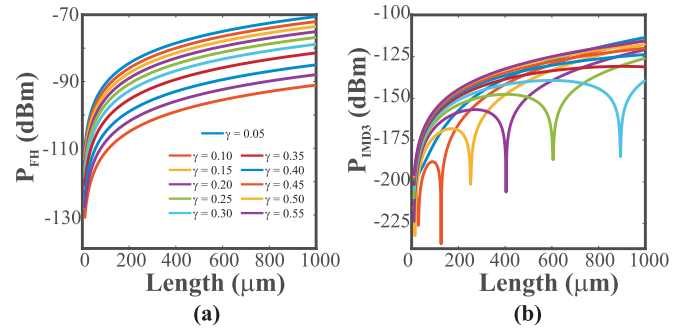

Fig. 9. Estimated power of (a) fundamental or first harmonic (FH) component; (b) IMD3 component with varying L, and γ. Note that the color legend is kept same.

TM modes compared to other metal combinations. Similar kind of results are also reported in [31], [32], [38]–[40]. Apart from the lower modal attenuation, the perturbation in r.i. for the noble metal based electrodes offer significant improved performance compared to Al or W-based electrodes (refer to Fig. 5). Thus, we have chosen the metal combination for the electrodes E1-E2-E3 is Au-Ag-Au. Also, many active silicon photonic devices are being recently reported with electrodes made of noble metals like Au [41]–[46] and Ag [47]–[52] making our proposed device suitable for future CMOS fabrication process if not now.

C. Steady State Performance

At first, we have estimated Δn and $\Delta \alpha$ as a function of applied bias voltage (V_{DC}) and then fitted 4th order polynomials to obtain $\Delta n(V)$, and $\Delta \alpha(V)$ as shown in Fig. 6. Using the fitted polynomials, and (6b), we have then estimated the steady state transfer function of a single sub-MZM. For simulation, we have considered the following simulation parameters: $L = 400$ μm, $\lambda = 1550$ nm, $P_{\text{in}} = 0$ dBm. The steady state transfer function of a single MZM (MZM-1) with the varying values of γ_1 (coupling coefficient of input coupler) is illustrated in Fig. 7. From the Fig. 7, it is evident that the transfer function of the single-MZM is almost sinusoidal and thus it will produce IMD components in the modulated output signal as predicted in Section II. Now to linearize the transfer function, another identical MZM is connected in series as shown in Fig. 1(a). The power splitting ratio of the RF power splitter and the transfer function of the cascaded structure is estimated. It must be noted that, the applied DC bias voltages ($V_{DC,i}$) are not varied. As a result, imbalance in the driving RF signals will produce different operating points of the two sub-MZMs. These different operating points of both sub-MZMs will cause one of the sub-MZM to offer higher ER compared to the other sub-MZM. As mentioned in Section I, this will force the cascaded structure to offer a linearized transfer function. In this study, we have varied the power imbalance in two sub-MZMs from 0 dB to 6 dB in a step of 1 dB. The obtained simulation result is shown in Fig. 8. As per the simulation results depicted in Fig. 8, the proposed cascaded modulator can offer approximately 16 dB of static

ER with 3 dB of insertion loss (IL). In such an operation, the voltage across the modulator should be varied between 2 V to 8 V approximately. Also, in the presence of RF signal, the performance of the modulator will improve if a suitable DC bias voltage ($\simeq 2$ V) is applied with the RF signal. From the simulation result, it is evident that the nonlinear behaviour of DC transfer function of the proposed modulator structure reduces with an increasing power imbalance between the two sub-MZMs. This reduction in nonlinear behaviour comes at the cost of a reduction in static ER. However, for a more improved performance we need to optimize L, γ_1, and γ_2 for the proposed dual series MZM. Optimization of L, γ_1, and γ_2 w.r.t. nonlinear performance of the cascaded modulator will be discussed in the next section.

D. Nonlinear Performance

For the simulation of the nonlinear performance of the proposed modulator, we have utilized the 4th order polynomial between Δn and V_{DC} as described shown in Fig. 6. The fitted coefficients are $k_1 = -9.737 \times 10^{-5}$, $k_2 = -3.972 \times 10^{-5}$, $k_3 = 3.653 \times 10^{-6}$, and $k_4 = -1.524 \times 10^{-7}$. We have then estimated power of the fundamental component and IMD3 component of the modulated output signal using the (12) assuming $v_0 = 1$ V and $P_{\text{in}} = 10$ dBm. In Fig. 9, we have plotted the
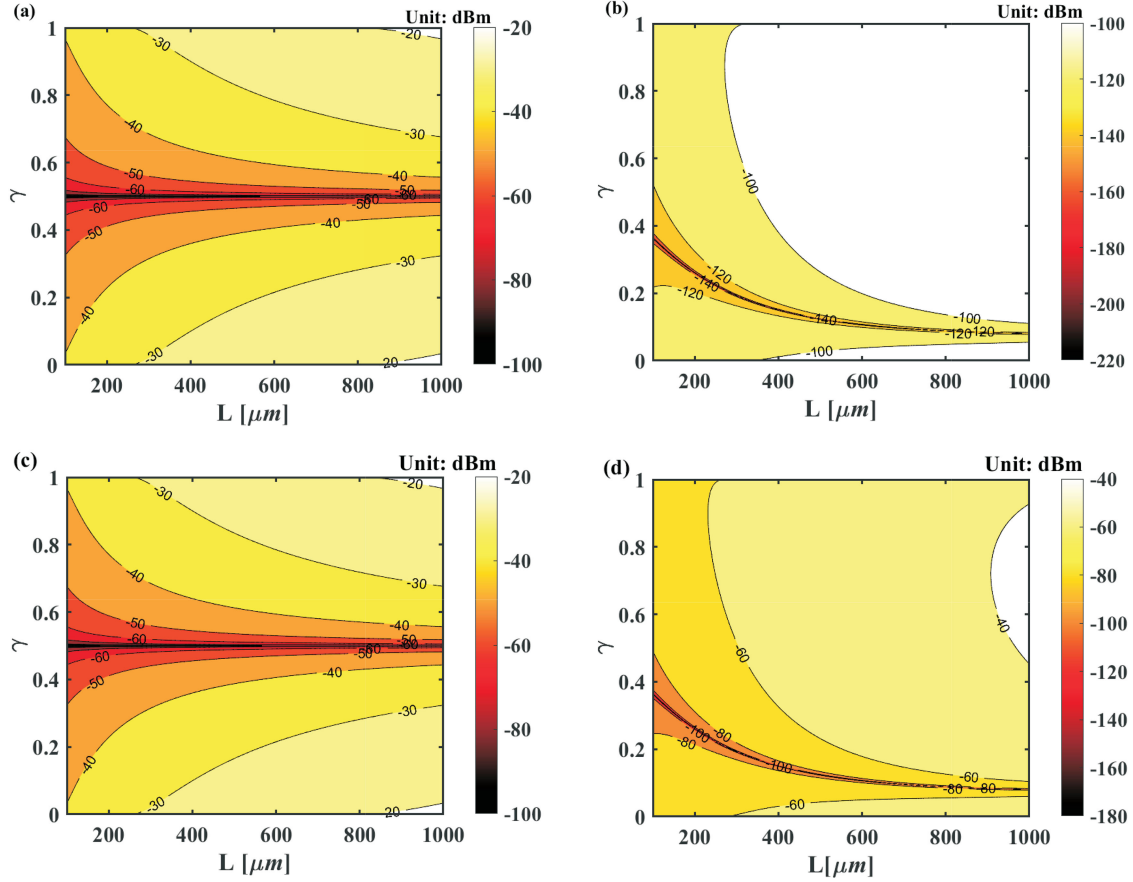
Fig. 10. Contour maps of (a-c) first-order harmonics (FH) and (b-d) IMD3 powers as a function of γ and L for the dual-series MZM. Parameters in the calculation are: $\lambda = 1550$ nm, $P_{\text{in}} = 10$ mW, v_0 is 0.2 V for (a-b) and 1 V for (c-d).

power of the fundamental and IMD3 component as a function of L, r_1, and r_2. It is important to note that r_1 and r_2 can be expressed in terms of power coupling coefficient as, $r_1 = \sqrt{\gamma}$ and $r_2 = \sqrt{1-\gamma}$ where γ is the power splitting ratio of the RF power splitter. In Fig. 9, we have varied γ between 0.05 to 0.55 in a step of 0.05. As evident from Fig. 9, we have estimated $P_{FH} = -82.93$ dBm and $P_{IMD3} = -206.1$ dBm for the proposed modulator with $L = 404$ μm and $\gamma = 0.20$. However, for $\gamma = 0.25$ and $L = 606$ μm, the estimated power of FH and IMD3 component of the modulated signals are -81.2 and -186.8 dBm, respectively. In Fig. 10, the contour plot of the RF power for fundamental or first-order harmonic and IMD3 are shown with varying L and γ. Two different RF signal amplitudes i.e. 0.2 V and 1.0 V is considered to depict the effect in FH and IMD3. The results show that the IMD3 component gets enhanced with increased v_0. However, such an increment in IMD3 strength can be tackled by choosing the proper values of γ and L.

In the previous analysis, we underestimated the nonlinear performance of the proposed modulator as the optical loss coefficient was neglected. However we have also performed the dual-tone test to estimate the SFDR for the second and third harmonics of the proposed modulator considering the loss coefficient. For simulation, two tones are located at 10 GHz and 10.00001 GHz (10 kHz of spacing), and the noise floor

of the spectrum analyzer is assumed at 156 dBm/Hz. The optical-to-electrical (OE) conversion is done by 30 GHz PIN photodetector with a responsivity of 0.85 A/W, while the dark current of the PIN PD is assumed to be 10 nA. The simulation is carried out using a commercial grade photonic integrated circuit simulator (ANSYS Lumerical Interconnect R2022). The simulated SFDR of a single MZM with $L = 775$ μm and the cascaded structure of the same MZM is shown in Fig. 11. As per the results shown in Fig. 11(a), the estimated SFDR of IMD2 and IMD3 for the single MZM are 92.65 dB.Hz$^{1/2}$ and 100.6 dB.Hz$^{2/3}$. Similarly from Fig. 11(b) the estimated value of IMD2 and IMD3 for the proposed dual-series MZM are approximately 96.11 dB.Hz$^{1/2}$ and 132.4 dB.Hz$^{2/3}$, respectively. The estimated SFDR results confirm the efficacy of the cascaded structure in terms of linearized operation of the proposed modulator.

E. Transient Performance

To estimate the transient performance, we have provided a $2^{31} - 1$ pseudorandom bit sequence (PRBS) as the electrical message signal in the proposed modulator with 2 dB imbalance in the electrical signal (refer to Fig. 8). The 20 Gb/s RF signal driving the proposed modulator with $L = 775$ μm has a peak-to-peak amplitude and DC offset voltage of 3 V and 2 V,
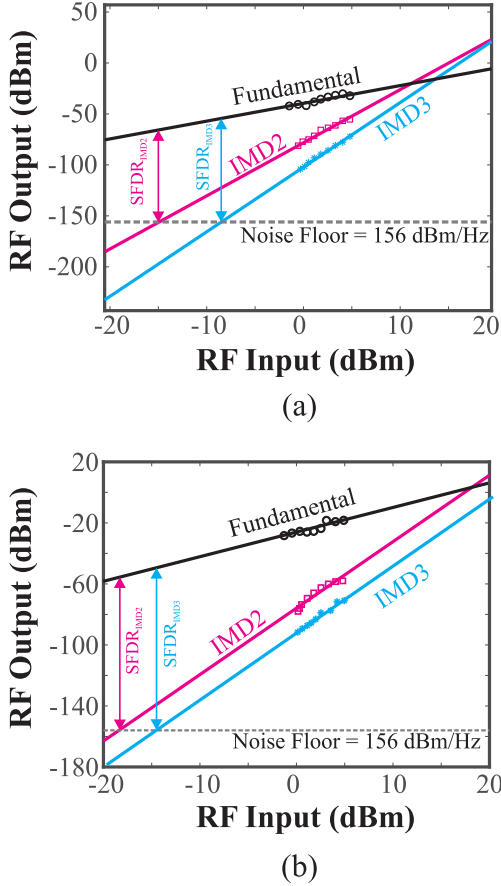
Fig. 11. Estimated SFDR of the proposed MZM: (a) single MZM; (b) dual-series MZM. Other simulation parameters are: $V_{DC} = 2V$, $P_{in} = 0$ dBm, $\lambda = 1550$ nm, RF signal frequency = 10 GHz.

Fig. 12. Transient performance of the proposed modulator with $L = 775 \ \mu m$ in the presence of $2^{31} - 1$ PRBS signal at 20 Gb/s data rate: amplitude vs. time after (a) MZM-1; (b) MZM-2; corresponding eye-diagram after (c) MZM-1; (d) MZM-2.

Fig. 13. Simulated electro-optic response of single MZM and dual-series MZM structure. The length of the both sub MZMs are 775 μm.

respectively. Modulated output optical signals after MZM-1 and MZM-2 are shown in Fig. 12(a)–(b). The eye diagrams after each MZM are shown in Fig. 12(c) and (d). From Fig. 12(a), we have estimated the dynamic ER at 20 Gb/s data rate offered by the modulator is approximately 4.06 dB. As we have cascaded two modulators for linearized operation, it is expected that the cascaded structure will offer decreased 3-dB electro-optic (EO) bandwidth compared to a single sub-MZM. We have performed EO simulation for a 775 μm long single MZM and found the 3-dB EO bandwidth to be 11.39 GHz. The cascaded structure offers a 3-dB EO bandwidth of 8.32 GHz (refer to Fig. 13). This reduction in 3-dB EO bandwidth can also be confirmed using the following relation.

$$f_{3-dB} = \left(\frac{1}{f_{3-dB,MZM-1}^2} + \frac{1}{f_{3-dB,MZM-2}^2} \right)^{-\frac{1}{2}} \quad (17)$$

EO simulation using Ansys Lumerical Interconnect also reveals the 3-dB EO bandwidth of the cascaded structure to be approximately 8.32 GHz, while the estimation from (17) is approximately 8.05 GHz. Therefore we conclude that the analytical and simulation results closely match.
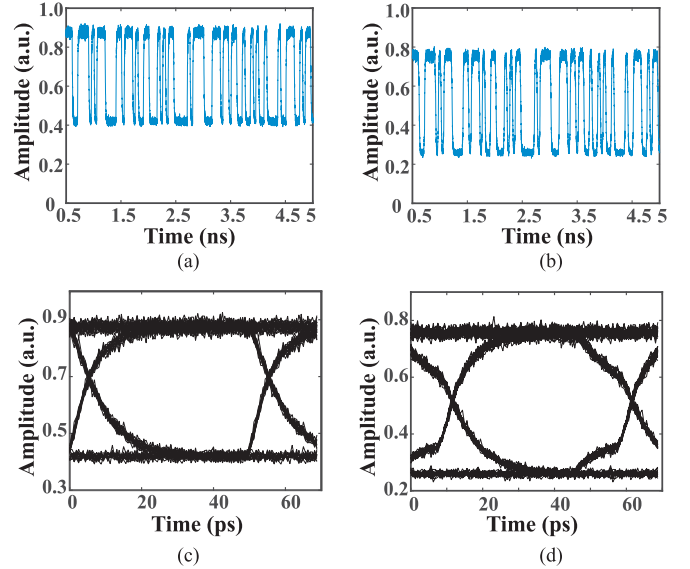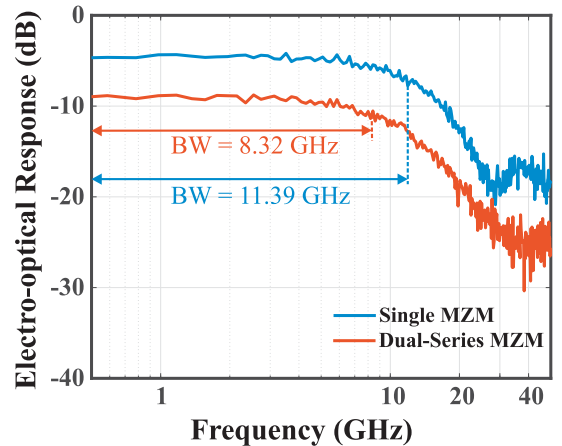
IV. CONCLUSION

In this paper, we have analyzed a dual series MZM based on two ED enabled MZMs. Detailed mathematical analysis on the transfer function and nonlinear performance of such a cascaded modulator is presented in this paper. Linearization of the proposed MZM based on electrical power imbalance is also discussed in the paper. The proposed modulator's operation is also supported by analysis. From the results, we can conclude that one can significantly improve the nonlinear performance of the proposed modulator by adjusting γ and L of the modulator. As an example we have shown that a significant suppression as high as 120 dB between the FH and IMD3 component is achievable for 404 μm long sub-MZM with $\gamma = 0.20$. Steady state simulation shows that the proposed modulator can offer 17 dB of ER for a DC voltage change of 6 V, approximately. A

2 dB electrical power imbalance between the two sub-MZMs is required to achieve the mentioned ER. The proposed modulator is found to offer offer 3.2 dB IL with 10.2 dB of dynamic ER at 10 Gb/s data rate. The dual tone test method estimated the SFDR of a single MZM with $L = 775$ μm for IMD2 and IMD3 are 92.65 dB.Hz$^{1/2}$ and 100.6 dB.Hz$^{2/3}$, respectively. Similar analysis for the dual-series MZM is carried out and the estimated SFDR for IMD2 and IMD3 are 96.11 dB.Hz$^{1/2}$ and 132.4 dB.Hz$^{2/3}$, respectively. Hence, the improvement in SFDR for IMD2 and IMD3 in the case of dual-series MZM are 3.46 dB and 31.8 dB, respectively. From the transient analysis, we have estimated the 3-dB EO bandwidth of the single MZM and dual-series MZM (both has $L = 775$ μm) are 11.39 GHz and 8.32 GHz, respectively. Thus, the linearisation of the dual-series MZM comes at the cost of 3-dB EO bandwidth. As the proposed dual series MZM offers high dynamic ER even at high data rates, it can be used as an silicon photonic PAM-4 modulator suitable for intra data centre communications. Also, the proposed linearized dual-series MZM can be used for analog-photnic link.

REFERENCES

[1] M. R. Tan *et al.*, "Universal photonic interconnect for data centers," *J. Lightw. Technol.*, vol. 36, no. 2, pp. 175–180, 2018.

[2] Z. Zhou, R. Chen, X. Li, and T. Li, "Development trends in silicon photonics for data centers," *Opt. Fiber Technol.*, vol. 44, pp. 13–23, 2018.

[3] S. Rumley *et al.*, "Optical interconnects for extreme scale computing systems," *Parallel Comput.*, vol. 64, pp. 65–80, 2017.

[4] C. A. Thraskias *et al.*, "Survey of photonic and plasmonic interconnect technologies for intra-datacenter and high-performance computing communications," *IEEE Commun. Surv. Tut.*, vol. 20, no. 4, pp. 2758–2783, Oct.–Dec. 2018.

[5] D. Marris-Morini *et al.*, "Recent progress in high-speed silicon-based optical modulators," *IEEE Proc. Instit. Radio Engineers*, vol. 97, no. 7, pp. 1199–1215, 2009.

[6] G. T. Reed *et al.*, "Recent breakthroughs in carrier depletion based silicon optical modulators," *Nanophotonics*, vol. 3, no. 4–5, pp. 229–245, 2014.

[7] J. Liu, G. Xu, F. Liu, I. Kityk, X. Liu, and Z. Zhen, "Recent advances in polymer electro-optic modulators," *Recursive Systematic Convolutional Adv.*, vol. 5, no. 21, pp. 15784–15794, 2015.

[8] J. Witzens, "High-speed silicon photonics modulators," *IEEE Proc. Instit. Radio Engineers*, vol. 106, no. 12, pp. 2158–2182, Dec. 2018.

[9] Z. Wang *et al.*, "Resonance control of a silicon micro-ring resonator modulator under high-speed operation using the intrinsic defect-mediated photocurrent," *Opt. Exp.*, vol. 25, no. 20, pp. 24827–24836, 2017.

[10] K. Padmaraju and K. Bergman, "Resolving the thermal challenges for silicon microring resonator devices," *Nanophotonics*, vol. 3, no. 4–5, pp. 269–281, 2014.

[11] S. Pal and S. Gupta, "Nonlinear performance and small signal model of junction-less microring modulator," *Opt. Commun.*, vol. 459, 2020, Art. no. 124984.

[12] W. M. Green, M. J. Rooks, L. Sekaric, and Y. A. Vlasov, "Ultra-compact, low RF power, 10 Gb/s silicon Mach-Zehnder modulator," *Opt. Exp.*, vol. 15, no. 25, pp. 17106–17113, 2007.

[13] H. Shu *et al.*, "Significantly high modulation efficiency of compact graphene modulator based on silicon waveguide," *Sci. Rep.*, vol. 8, no. 1, pp. 1–8, 2018.

[14] B. Wang *et al.*, "Modulation on silicon for datacom: Past, Present, and Future," *Prog. Electromagnetics Res.*, vol. 166, pp. 119–145, 2019.

[15] S. M. Sze and K. K. Ng, *Physics of Semiconductor Devices*. New York, NY, USA: Wiley, 2006.

[16] Y. Taur and T. H. Ning, *Fundamentals of Modern VLSI Devices*. New York, NY, USA: Cambridge Univ. Press, 2013.

[17] C. Shin *et al.*, *Variation-Aware Advanced CMOS Devices and SRAM*. vol. 56, Berlin, Germany: Springer, 2016.

[18] C. Shin, X. Sun, and T.-J. K. Liu, "Study of random-dopant-fluctuation (RDF) effects for the trigate bulk mosfet," *IEEE Trans. Electron Devices*, vol. 56, no. 7, pp. 1538–1542, Jul. 2009.

[19] S. Pal and S. Gupta, "Performance analysis of an electrostatic doping assisted silicon microring modulator," *Opt. Commun.*, vol. 430, pp. 131–138, 2019.

[20] S. Pal and S. Gupta, "Junction-less optical phase shifter loaded silicon Mach-Zehnder modulator," *Opt. Commun.*, vol. 437, pp. 110–120, 2019.

[21] S. Pal, P. K. Tiwari, and S. Gupta, "A proposal for an electrostatic doping-assisted electroabsorption modulator for intrachip communication," *IEEE Trans. Electron Devices*, vol. 66, no. 5, pp. 2269–2275, May 2019.

[22] M. Nedeljkovic, R. Soref, and G. Z. Mashanovich, "Free-carrier electrorefraction and electroabsorption modulation predictions for silicon over the 1–14-μm infrared wavelength range," *IEEE Photon. J.*, vol. 3, no. 6, pp. 1171–1180, Dec. 2011.

[23] L. Chrostowski and M. Hochberg, *Silicon Photonics Design: From Devices to Systems*, New York, NY, USA: Cambridge Univ. Press, 2015.

[24] G. E. Betts, "Linearized modulator for suboctave-bandpass optical analog links," *IEEE Trans. Microw. Theory Techn.*, vol. 42, no. 12, pp. 2642–2649, Dec. 1994.

[25] W. K. Burns, "Linearized optical modulator with fifth order correction," *J. Lightw. Technol.*, vol. 13, no. 8, pp. 1724–1727, 1995.

[26] X. Zhu *et al.*, "Linearization of two cascaded intensity-modulator-based analog photonic link," *Opt. Eng.*, vol. 57, no. 8, 2018, Art. no. 080501.

[27] C. G. Bottenfield, V. Thomas, and S. E. Ralph, "Silicon photonic modulator linearity and optimization for microwave photonic links," *IEEE J. Sel. Topics Quantum Electron.*, vol. 25, no. 5, pp. 1–10, Sep./Oct. 2019.

[28] W. Shi, Y. Xu, H. Sepehrian, S. LaRochelle, and L. Rusch, "Silicon photonic modulators for PAM transmissions," *J. Opt.*, vol. 20, 2018, Art. no. 083002.

[29] Q. Zhang *et al.*, "Linearity comparison of silicon carrier-depletion-based single, dual-parallel, and dual-series Mach-Zehnder modulators," *J. Lightw. Technol.*, vol. 36, no. 16, pp. 3318–3331, 2018.

[30] R. J. Hueting, B. Rajasekharan, C. Salm, and J. Schmitz, "The charge plasma PN diode," *IEEE Electron Device Lett.*, vol. 29, no. 12, pp. 1367–1369, Dec. 2008.

[31] M. Alam, J. S. Aitchison, and M. Mojahedi, "Compact and silicon-on-insulator-compatible hybrid plasmonic te-pass polarizer," *Opt. Lett.*, vol. 37, no. 1, pp. 55–57, 2012.

[32] M. Alam, J. S. Aitchison, and M. Mojahedi, "Theoretical analysis of hybrid plasmonic waveguide," *IEEE J. Sel. Topics Quantum Electron.*, vol. 19, no. 3, pp. 4602008–4602008, May/Jun. 2013.

[33] X. Li, F. Yang, F. Zhong, Q. Deng, J. Michel, and Z. Zhou, "Single-drive high-speed lumped depletion-type modulators toward 10 fJ/bit energy consumption," *Photon. Res.*, vol. 5, no. 2, pp. 134–142, 2017.

[34] A. M. Gutierrez *et al.*, "Analytical model for calculating the nonlinear distortion in silicon-based electro-optic Mach-Zehnder modulators," *J. Lightw. Technol.*, vol. 31, no. 23, pp. 3603–3613, 2013.

[35] J. Ding, S. Shao, L. Zhang, X. Fu, and L. Yang, "Method to improve the linearity of the silicon Mach-Zehnder optical modulator by doping control," *Opt. Exp.*, vol. 24, no. 21, pp. 24641–24648, 2016.

[36] F. Grillot, L. Vivien, S. Laval, and E. Cassan, "Propagation loss in single-mode ultrasmall square silicon-on-insulator optical waveguides," *J. Lightw. Technol.*, vol. 24, no. 2, 2006, Art. no. 891.

[37] Lumerical device r2018a r3. [Online]. Available: http://www.lumerical.com/tcad-products/device/

[38] J. Wang *et al.*, "Sub-μm^2 power splitters by using silicon hybrid plasmonic waveguides," *Opt. Exp.*, vol. 19, no. 2, pp. 838–847, 2011.

[39] J. Chee, S. Zhu, and G. Lo, "CMOS compatible polarization splitter using hybrid plasmonic waveguide," *Opt. Exp.*, vol. 20, no. 23, pp. 25345–25355, 2012.

[40] D. Dai and S. He, "Low-loss hybrid plasmonic waveguide with double low-index nano-slots," *Opt. Exp.*, vol. 18, no. 17, pp. 17958–17966, 2010.

[41] M.-S. Kwon, "Metal-insulator-silicon-insulator-metal waveguides compatible with standard CMOS technology," *Opt. Exp.*, vol. 19, no. 9, pp. 8379–8393, 2011.

[42] I. Datta *et al.*, "Low-loss composite photonic platform based on 2D semiconductor monolayers," *Nature Photon.*, vol. 14, no. 4, pp. 256–262, 2020.

[43] M. Nielsen, A. Ashfar, K. Cadien, and A. Elezzabi, "Plasmonic materials for metal-insulator-semiconductor-insulator-metal nanoplasmonic waveguides on silicon-on-insulator platform," *Opt. Mater.*, vol. 36, no. 2, pp. 294–298, 2013.

[44] G. Sinatkas, T. Christopoulos, O. Tsilipakos, and E. E. Kriezis, "Electro-optic modulation in integrated photonics," *J. Appl. Phys.*, vol. 130, no. 1, 2021, Art. no. 010901.

[45] A. A. Demkov, C. Bajaj, J. G. Ekerdt, C. J. Palmstrøm, and S. Ben Yoo, "Materials for emergent silicon-integrated optical computing," *J. Appl. Phys.*, vol. 130, no. 7, 2021, Art. no. 070907.

[46] P. Steglich *et al.*, "Silicon-organic hybrid photonics: An overview of recent advances, electro-optical effects and CMOS integration concepts," *J. Physics: Photon.*, vol. 3, no. 2, 2021, Art. no. 022009.

[47] J. Du and J. Wang, "Hybrid plasmonic microring nano-ruler," *Sci. Rep.*, vol. 8, no. 1, pp. 1–7, 2018.

[48] M. Lu *et al.*, "Ultra-compact TE-mode-pass power splitter based on sub-wavelength gratings and hybrid plasmonic waveguides on SOI platform," *Opt. Commun.*, vol. 498, 2021, Art. no. 127250.

[49] P. Sharma and D. K. Vishwakarma, "Long range multilayer hybrid plasmonic waveguide components and integrated circuit," *IEEE Trans. Nanotechnol.*, vol. 18, pp. 940–947, 2019.

[50] L. Shirafkan Dizaj, K. Abbasian, and T. Nurmohammadi, "A three-core hybrid plasmonic polarization splitter designing based on the hybrid plasmonic waveguide for utilizing in optical integrated circuits," *Plasmonics*, vol. 15, no. 6, pp. 2213–2221, 2020.

[51] K. Li *et al.*, "Nanoscale light confinement and nonlinearity of hybrid plasmonic waveguide with a metal cap," *Opt. Eng.*, vol. 54, no. 10, 2015, Art. no. 107101.

[52] H. Zhang, F. Zhang, Y. Liang, X.-G. Huang, and B. Jia, "Diodelike asymmetric transmission in hybrid plasmonic waveguides via breaking polarization symmetry," *J. Phys. D: Appl. Phys.*, vol. 50, no. 16, 2017, Art. no. 165104.